

Banner appropriate to article type will appear here in typeset article

# Nested traveling wave structures in elastoinertial turbulence

Manish Kumar<sup>1</sup> and Michael D. Graham<sup>1</sup>†

<sup>1</sup>Department of Chemical and Biological Engineering, University of Wisconsin-Madison, 1415 Engineering Dr, Madison, WI 53706, USA

(Received xx; revised xx; accepted xx)

Elastoinertial turbulence (EIT) is a chaotic flow resulting from the interplay between inertia and viscoelasticity in wall-bounded shear flows. Understanding EIT is important because it is thought to set a limit on the effectiveness of turbulent drag reduction in polymer solutions. Here, we analyze simulations of two-dimensional EIT in channel flow using Spectral Proper Orthogonal Decomposition (SPOD), discovering a family of traveling wave structures that capture the sheetlike stress fluctuations that characterize EIT. The frequency-dependence of the leading SPOD mode contains distinct peaks and the mode structures corresponding to these peaks exhibit well-defined traveling structures. The structure of the dominant traveling mode exhibits shift-reflect symmetry similar to the viscoelasticity-modified Tollmien–Schlichting (TS) wave, where the velocity fluctuation in the traveling mode is characterized by large-scale regular structures spanning the channel and the polymer stress field is characterized by thin, inclined sheets of high polymer stress localized at the critical layers near the channel walls. The traveling structures corresponding to the higher-frequency modes have a very similar structure, but are nested in a region roughly bounded by the critical layer positions of the next-lower frequency mode. A simple theory based on the idea that the critical layers of mode  $\kappa$  form the “walls” for the structure of mode  $\kappa + 1$  yields quantitative agreement with the observed wave speeds and critical layer positions, indicating self-similarity between the structures. The physical idea behind this theory is that the sheetlike localized stress fluctuations in the critical layer prevent velocity fluctuations from penetrating them.

## 1. Introduction

Adding a tiny amount of high molecular weight polymer to a fluid dramatically reduces turbulent drag (Toms 1949). Therefore, the polymer additives are used to reduce pumping costs in pipeline transport of crude oil and home heating and cooling systems, and to reduce fuel transfer time in airplane tank filling (Brostow 2008). Polymer additives also have been envisioned for flood remediation and enhancement of the drainage capacity of sewer systems (Kumar & Graham 2023; Bouchenafa *et al.* 2021; Sellin 1978). Newtonian turbulent flow contains streamwise vortices close to walls, which dominate the near-wall momentum transport and thus the drag. During drag reduction, the polymer chains get stretched due to turbulence, leading to stress distributions that wrap around the streamwise

† Email address for correspondence: mdgraham@wisc.edu

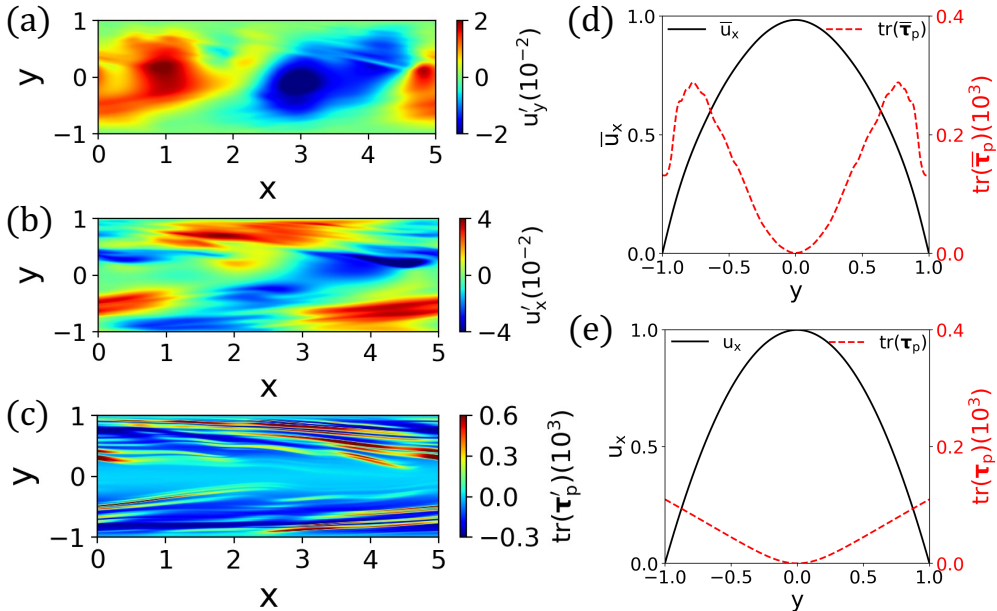


Figure 1: Snapshots of perturbations of (a) wall-normal velocity ( $u'_y$ ), (b) streamwise velocity ( $u'_x$ ), and (c) trace of the polymer stress tensor ( $\text{tr}(\boldsymbol{\tau}'_p)$ ) from their temporal arithmetic means in EIT. (d) Profiles of mean streamwise velocity ( $\bar{u}_x$ ) and mean of the trace of polymer stress tensor ( $\text{tr}(\bar{\boldsymbol{\tau}}_p)$ ) in EIT. (e) Profiles of streamwise velocity and the trace of the polymer stress tensor in the unidirectional laminar flow state. For all plots,  $Re = 3000$  and  $Wi = 35$ . The variables have been nondimensionalized with their respective scales (see Section 2).

vortices, weakening them to lead to lower turbulent drag (Li & Graham 2007; Kim *et al.* 2007; Graham & Floryan 2021).

However, this suppression of near-wall vortices does not generally lead to full relaminarization, but rather to a limiting state called the maximum drag reduction (MDR) asymptote. Some understanding of this observation has come from the discovery of elastoinertial turbulence (EIT), a complex chaotic flow that is sustained, rather than suppressed by viscoelasticity, and thus helps explain the absence of relaminarization (Samanta *et al.* 2013; Dubief *et al.* 2023; Shekar *et al.* 2019). Nevertheless, the structure and mechanism underlying EIT remain poorly understood and are the topic of the present work.

EIT and MDR arise in parameter regimes of Reynolds number  $Re$  and Weissenberg number  $Wi$  (product of polymer relaxation time and nominal strain rate) where the unidirectional laminar flow is linearly stable and is thus a nonlinearly self-sustaining flow. The basic structure in both channel and pipe flows (Samanta *et al.* 2013; Lopez *et al.* 2019) is two-dimensional (2D) (Sid *et al.* 2018), characterized by vorticity fluctuations localized in narrow regions near the walls with tilted sheets of highly stretched polymers emanating from these regions. Figure 1 shows snapshots of velocity and polymeric stress fields of a simulated 2D EIT in channel flow along with their temporal mean profiles in EIT and the corresponding profiles in the unidirectional laminar state.

Despite the absence of an obvious linear instability mechanism for EIT, it has been hypothesized that EIT is related to the nonlinear excitation of either a “wall mode” or a “center mode” structure arising in the linear stability problem for the unidirectional laminar state (Drazin & Reid 1981; Datta *et al.* 2022). A wall mode has a wave speed much less

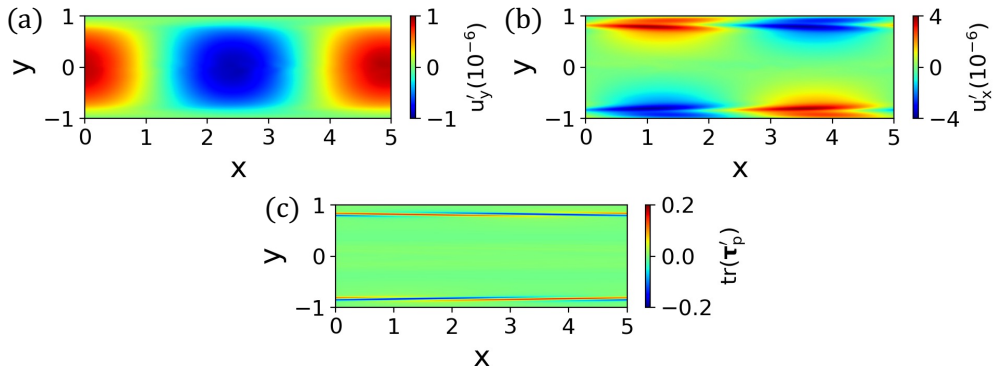


Figure 2: Structures of the perturbations of (a) wall-normal velocity ( $u'_y$ ), (b) streamwise velocity ( $u'_x$ ), and (c) trace of polymer stress tensor ( $\text{tr}(\boldsymbol{\tau}'_p)$ ) from the unidirectional laminar state for the viscoelastic linear TS wave at  $Re = 3000$  and  $Wi = 35$ . This mode ultimately vanishes as viscoelastic channel flow is linearly stable at this parameter regime.

than the centerline velocity, and critical layer positions, i.e. where the wave speed equals the local laminar velocity, near the walls. In contrast, a center mode travels at nearly the centerline velocity and accordingly the critical layer position is near the centerline. The Tollmien-Schlichting (TS) mode of classical linear analysis of plane Poiseuille flow is a wall mode, and there is a strong structural resemblance of the viscoelastic extension of the TS wave to EIT (Shekar *et al.* 2019, 2020, 2021). Figure 2 shows the viscoelastic linear TS mode at the same conditions as Figure 1. Since the laminar state at these conditions is linearly stable, a sufficiently small random perturbation will decay, with the slowest mode of decay having this form. Sheets of highly stretched polymer are generated in the TS wave due to the presence of hyperbolic stagnation points (in the frame traveling with the wave) in the Kelvin cat's-eye structure of the velocity field in the critical layer (Shekar *et al.* 2019). The recently discovered “polymer diffusive instability (PDI)” is also a wall mode (Beneitez *et al.* 2023; Couchman *et al.* 2024). However, in the parameter regime considered in the present study, the PDI does not arise; the laminar profile is linearly stable, and accordingly simulations with initial conditions that are very small perturbations from laminar flow decay back to it. The possibility of a center mode structure is of interest in part because there is a linear center mode instability at low Reynolds number  $Re$  that may organize “elastic turbulence” at very small Reynolds number  $Re$  (Garg *et al.* 2018; Khalid *et al.* 2021; Choueiri *et al.* 2021; Morozov 2022). Nevertheless, in the elastoinertial regime considered here, while center mode structures can exist (Dubief *et al.* 2022), they do not appear to play an active role in the structure and self-sustenance of EIT (Beneitez *et al.* 2024). The present work is consistent with this picture, and indeed deepens the connection between EIT and wall modes, showing in particular the existence of a nested family of such structures.

In the present study, we investigate the structure and dynamics of EIT in channel flow using a modal decomposition technique known as spectral proper orthogonal decomposition (SPOD) (Towne *et al.* 2018). SPOD characterizes coherent structures in complex flows that have well-defined structures and persist both in space and time via a frequency-domain variant of Proper Orthogonal Decomposition (POD) (Lumley 1967). At a given frequency, SPOD generates an energetically ordered and spatially orthogonal set of modes characterizing the flow. The modes and eigenvalues obtained using SPOD analysis can be interpreted as physical structures with a particular frequency and the energies associated with those structures (Schmidt & Towne 2019). SPOD and dynamic mode decomposition (DMD) are

related, as detailed in Towne *et al.* (2018). In particular, DMD gives modes that correspond to particular frequencies. However, in DMD, there is no natural ordering of modes; in contrast, SPOD gives at each frequency an orthogonal basis set of modes ordered by their mean-square contribution to the flow at that frequency.

SPOD has been successfully used in inertial turbulence to understand coherent structures and develop a low-dimensional model for turbulence (Schmidt *et al.* 2017; Araya *et al.* 2017; Tutkun & George 2017; Braud *et al.* 2004; Hellström & Smits 2014; Nekkanti & Schmidt 2021). Here, we use it to investigate traveling coherent structures underlying the chaotic dynamics of EIT. We will focus on the frequency-dependence of the most energetic SPOD mode, as it reveals important coherent features of the flow.

## 2. Formulation and governing equations

Because the self-sustaining dynamics of elastoinertial turbulence are fundamentally 2D (Sid *et al.* 2018), we consider two-dimensional (2D) viscoelastic channel flow with nondimensional equations of mass and momentum conservation:

$$\nabla \cdot \mathbf{u} = 0, \quad \frac{\partial \mathbf{u}}{\partial t} + \mathbf{u} \cdot \nabla \mathbf{u} = -\nabla p + \frac{\beta}{Re} \nabla^2 \mathbf{u} + \frac{1-\beta}{Re} \nabla \cdot \boldsymbol{\tau}_p + f(t) \mathbf{e}_x, \quad (2.1)$$

where  $\mathbf{u}$  and  $p$  are non-dimensional velocity field and pressure field, respectively. Newtonian laminar centerline velocity ( $U_c$ ) and channel half width ( $H$ ) have been used as characteristic velocity scale and length scale, respectively. The ratio between solvent viscosity ( $\eta_s$ ) to zero shear rate solution viscosity ( $\eta$ ) has been denoted by  $\beta = \eta_s/\eta$ . The Reynolds number has been defined as  $Re = \rho U_c H/\eta$ , where  $\rho$  represents fluid density. We use no-slip boundary conditions for the velocity field at the channel wall. Periodic boundary conditions have been used at the inlet and outlet of the channel. Flow is driven by an external forcing term  $f(t) \mathbf{e}_x$ , where  $\mathbf{e}_x$  denotes the streamwise direction. The forcing term varies with time to keep the bulk velocity ( $U_b = 2U_c/3$ ) at its Newtonian laminar value. The polymer stress tensor is denoted  $\boldsymbol{\tau}_p$  and we choose the FENE-P constitutive model with an artificial diffusion term to model its evolution:

$$\frac{\partial \boldsymbol{\alpha}}{\partial t} + \mathbf{u} \cdot \nabla \boldsymbol{\alpha} - \boldsymbol{\alpha} \cdot \nabla \mathbf{u} - (\boldsymbol{\alpha} \cdot \nabla \mathbf{u})^T = -\boldsymbol{\tau}_p + \frac{1}{ReSc} \nabla^2 \boldsymbol{\alpha}, \quad (2.2)$$

$$\boldsymbol{\tau}_p = \frac{1}{Wi} \left( \frac{\boldsymbol{\alpha}}{1 - \text{tr}(\boldsymbol{\alpha})/b} - I \right), \quad (2.3)$$

where  $\boldsymbol{\alpha}$  is the conformation tensor and parameter  $b$  characterizes the maximum extensibility of the polymer chains. The polymer stress tensor is nondimensionalized with  $\eta U_c/H$ . The Weissenberg number  $Wi = \lambda U_c/H$ , where  $\lambda$  is the polymer relaxation time. The Schmidt number  $Sc = \eta/\rho D$ , where  $D$  is the diffusion coefficient, represents the ratio of momentum diffusivity to mass diffusivity. The artificial diffusion term is used to stabilize the numerical scheme during the integration of Eq. 2.2. The presence of this term leads to the requirement of boundary conditions for the conformation tensor. At the channel walls, we determine  $\boldsymbol{\alpha}$  by solving the governing equations considering  $Sc \rightarrow \infty$ .

We solve the governing equations with a spectral method using the Dedalus framework (Burns *et al.* 2020). The computational domain has a length  $L = 5$ . The governing equations have been discretized using 256 Fourier basis functions and 1024 Chebyshev basis functions in the streamwise ( $x$ ) and wall-normal ( $y$ ) directions, respectively. We use  $\beta = 0.97$ ,  $b = 6400$ ,  $Re = 3000 - 6000$ , and  $Wi = 35 - 70$ , which are relevant to turbulent drag reduction and are in the range of values used in previous studies, e.g. (Shekar *et al.* 2019; Dubief *et al.* 2022). In reality, the Schmidt number for a polymer solution is very large ( $Sc \sim 10^6$ ). Numerical

simulation with such a large value of  $Sc$  would require an extremely fine mesh and small time-step, making numerical simulations computationally very expensive. At the same time, small  $Sc$  (i.e.,  $Sc < 10$ ) smears out small-scale dynamics and suppresses EIT (Sid *et al.* 2018; Dubief *et al.* 2023). Therefore, numerical simulations of EIT based on artificial diffusion generally use  $Sc \sim O(100)$  (Sid *et al.* 2018; Buza *et al.* 2022). In the present study, we use  $Sc = 250$  which is sufficient to sustain EIT and also numerically tractable. Viscoelastic channel flow in the parameter regime considered here is linearly stable. Therefore, to trigger EIT, we use unidirectional laminar flow with sufficiently large random perturbations in the conformation tensor as the initial condition of the simulation. In computing statistics, initial transients are dropped so that we consider only statistically stationary results.

To estimate the SPOD spectrum, the spatiotemporal state variables are organized in a vector  $\mathbf{q}(\mathbf{x}, t)$ . Here, we separately take this vector to contain wall-normal velocity, streamwise velocity, or the trace of the polymer stress tensor, as further discussed below. For a statistically stationary flow, the SPOD analysis can be done in Fourier space, where  $\tilde{\mathbf{q}}(\mathbf{x}, f)$  denotes the Fourier-transformed dataset. Notation and methodology here follow Towne *et al.* (2018). Given an inner product

$$\langle \tilde{\mathbf{q}}, \boldsymbol{\psi} \rangle = \int_{\Omega} \boldsymbol{\psi}^*(\mathbf{x}, f) \tilde{\mathbf{q}}(\mathbf{x}, f) d\mathbf{x} \quad (2.4)$$

where  $(^*)$  denotes conjugate transpose, the SPOD seeks to find a function  $\boldsymbol{\psi}(\mathbf{x}, f)$  that maximizes

$$E\{|\langle \tilde{\mathbf{q}}(\mathbf{x}, f), \boldsymbol{\psi}(\mathbf{x}, f) \rangle|^2\} \quad (2.5)$$

given the constraint  $\langle \boldsymbol{\psi}(\mathbf{x}, f), \boldsymbol{\psi}(\mathbf{x}, f) \rangle = 1$ , where  $\boldsymbol{\psi}(\mathbf{x}, f)$  is the SPOD mode at frequency  $f$ . The operators  $E\{\cdot\}$  and  $|\cdot|$  represent expectation and modulus, respectively. The maximization of Eq. 2.5 leads to the following eigenvalue problem:

$$\int_{\Omega} \mathbf{S}(\mathbf{x}, \mathbf{y}, f) \boldsymbol{\psi}(\mathbf{y}, f) d\mathbf{y} = \sigma(f) \boldsymbol{\psi}(\mathbf{x}, f), \quad (2.6)$$

where the cross-spectral density tensor  $\mathbf{S}$  is

$$\mathbf{S}(\mathbf{x}, \mathbf{y}, f) = E\{\tilde{\mathbf{q}}(\mathbf{x}, f) \tilde{\mathbf{q}}^*(\mathbf{y}, f)\}. \quad (2.7)$$

This eigenvalue problem (Eq. 2.6) leads to an infinite set of eigenmodes  $\{\sigma_j(f), \boldsymbol{\psi}_j(\mathbf{x}, f)\}$  at each frequency, which are generally arranged in decreasing order of  $\sigma_j$ . These eigenvalues are often called “energies”, because in the case where the time series is velocity, each eigenvalue indicates the amount of kinetic energy associated with the associated mode. The eigenvectors ( $\boldsymbol{\psi}_j$ ) are orthogonal and provide a complete basis for  $\tilde{\mathbf{q}}$ . Therefore, the Fourier-transformed dataset at a given frequency can be written in terms of SPOD modes as

$$\tilde{\mathbf{q}}(\mathbf{x}, f) = \sum_{j=1}^{\infty} a_j(f) \boldsymbol{\psi}_j(\mathbf{x}, f), \quad (2.8)$$

where  $a_j(f) = \langle \tilde{\mathbf{q}}(\mathbf{x}, f), \boldsymbol{\psi}_j(\mathbf{x}, f) \rangle$  are the SPOD coefficients.

To calculate the SPOD of a discrete time series of  $N_t$  snapshots  $\{\mathbf{q}(t_1), \mathbf{q}(t_2), \dots, \mathbf{q}(t_{N_t})\}$ , first, a data matrix  $\mathbf{Q}$  is constructed as:

$$\mathbf{Q} = [\mathbf{q}_1, \mathbf{q}_2, \dots, \mathbf{q}_{N_t}], \quad (2.9)$$

where  $\mathbf{q}_i = \mathbf{q}(t_i)$ . Multiple realizations of the flow field are generated by dividing the data matrix into overlapping blocks (Welch 1967)

$$\mathbf{Q}^n = [\mathbf{q}_1^n, \mathbf{q}_2^n, \dots, \mathbf{q}_m^n, \dots, \mathbf{q}_{N_f}^n], \quad n = 1, 2, \dots, N_b, \quad (2.10)$$

where  $N_f$  is the number of snapshots in each block. The total number of blocks can be given as  $N_b = (N_t - N_o)/(N_f - N_o)$ , where  $N_o$  represents the number of overlapping snapshots. The  $m^{th}$  entry in the  $n^{th}$  block ( $\mathbf{q}_m^n$ ) can be connected with the entry in  $\mathbf{Q}$  as  $\mathbf{q}_m^n = \mathbf{q}_{m+(n-1)(N_f-N_o)}$ . The non-periodicity of the data in each block may lead to spectral leakage during the estimation of the discrete Fourier transform (DFT). Therefore, to reduce the spectral leakage we compute the DFT of the windowed data:

$$\mathbf{Q}^{n,w} = [w_1 \mathbf{q}_1^n, w_2 \mathbf{q}_2^n, \dots, w_m \mathbf{q}_m^n, \dots, w_{N_f} \mathbf{q}_{N_f}^n], \quad (2.11)$$

where  $w_m$  is the nodal value of the symmetric Hamming window function:

$$w_m = 0.54 - 0.46 \cos\left(\frac{2\pi(m-1)}{N_f-1}\right). \quad (2.12)$$

The discrete Fourier transform of  $\mathbf{Q}^{n,w}$  gives

$$\tilde{\mathbf{Q}}^n = [\tilde{\mathbf{q}}_1^n, \tilde{\mathbf{q}}_2^n, \dots, \tilde{\mathbf{q}}_m^n, \dots, \tilde{\mathbf{q}}_{N_f}^n], \quad (2.13)$$

where  $\tilde{\mathbf{q}}_m^n$  represents the Fourier component at frequency  $f_m$  in the  $n^{th}$  block. Next, the data matrix is organized frequency-wise, where the Fourier components at frequency  $f_m$  from all the blocks are collected as

$$\tilde{\mathbf{Q}}_m = [\tilde{\mathbf{q}}_m^1, \tilde{\mathbf{q}}_m^2, \dots, \tilde{\mathbf{q}}_m^{N_b}]. \quad (2.14)$$

Now, the SPOD modes,  $\boldsymbol{\psi}_m$ , and energies,  $\boldsymbol{\sigma}_m$ , at the frequency  $f_m$  can be obtained by computing the eigenvectors and eigenvalues of the discretized cross-spectral density (CSD) matrix  $\mathbf{S}_m = \tilde{\mathbf{Q}}_m \tilde{\mathbf{Q}}_m^*$  by solving the eigenvalue problem

$$\mathbf{S}_m \mathbf{W} \boldsymbol{\psi}_m = \boldsymbol{\psi}_m \boldsymbol{\sigma}_m, \quad (2.15)$$

where  $\mathbf{W}$  is a positive-definite weighting matrix, which properly accounts for the numerical quadrature for integration on a non-uniform discrete grid, and  $\boldsymbol{\sigma}_m$  is a diagonal matrix of eigenvalues. This equation is the discretized version of (2.6). In practice, the number of flow realizations ( $N_b$ ) is much smaller than the number of grid points. Therefore, for faster computation, the eigenvalue problem

$$\tilde{\mathbf{Q}}_m^* \mathbf{W} \tilde{\mathbf{Q}}_m \boldsymbol{\theta}_m = \boldsymbol{\theta}_m \boldsymbol{\sigma}_m \quad (2.16)$$

is solved. This has the same nonzero eigenvalues as (2.15), and its eigenvectors are related to those of (2.15) by the expression

$$\boldsymbol{\psi}_m = \tilde{\mathbf{Q}}_m \boldsymbol{\theta}_m \boldsymbol{\sigma}_m^{-1/2}. \quad (2.17)$$

For the SPOD analysis, we use the MATLAB tool developed by Schmidt (2022). Details of the method and its numerical implementation can be found in literature (Towne *et al.* 2018; Schmidt & Colonius 2020). We use 600 time units of data generated using EIT simulation to perform SPOD analysis, which is sufficient for the convergence of SPOD. The dataset consists of  $N_t = 8000$  snapshots, which are sampled at the interval of  $\Delta t_s = 0.075$  time units. In the present study, we use  $N_f = 500$  snapshots in each block with 50% overlap ( $N_o = 250$ ), which leads to a total of  $N_b = 31$  blocks. The SPOD spectra estimated using different combinations of  $N_f$  and  $N_o$  have been shown in Appendix A. The number of modes obtained in SPOD is the same as the number of blocks, where the first mode has the highest energy and the last mode has the lowest energy. The number of non-negative frequencies is given by  $N_f/2 + 1$  and the interval between discrete consecutive frequencies is  $\Delta f = 1/(\Delta t_s N_f)$ .

### 3. Results and discussion

This study focuses on the case  $Re = 3000$ ,  $Wi = 35$ , for which a snapshot of perturbation of wall-normal velocity  $u'_y$ , streamwise velocity  $u'_x$ , and the trace of the polymer stress tensor  $\text{tr}(\boldsymbol{\tau}'_p)$  are shown in Figure 1, where (') represents the perturbation from the temporal arithmetic mean. We have also plotted mean and laminar profiles of different state variables in Figure 1. Note that the trace of the polymer stress field is closely related to the degree of polymer stretching, which is proportional to  $\text{tr}(\boldsymbol{\alpha})$ . The dynamics of  $u'_y$  in EIT are dominated by the downstream advection of large-scale structures spanning the channel (Fig. 1a and Supplementary video: Movie1) and the dynamics of  $u'_x$  are dominated by the downstream advection of structures localized close to the channel walls (Fig. 1b and Supplementary video: Movie2). The dynamics of the polymer stress field are dominated by the downstream motion of thin inclined sheets of polymer stress in the vicinity of the channel walls (Fig. 1c and Supplementary video: Movie3). Since wall-normal velocity is identically zero in the laminar state, its temporal mean is also identically zero so it yields the cleanest Fourier and SPOD spectra. We note that the velocity fluctuations at EIT are generally quite small (e.g.  $u'_y \sim 10^{-2}$  and drag is only 12.8% higher than the laminar), so the streamwise velocity profile does not greatly differ from laminar and hence it remains the dominant component of velocity (Fig. 1). The trace of the polymer stress tensor represents the contribution of polymer chains in the stress field, which regulates the flow field. Therefore,  $u'_y$ ,  $u'_x$ ,  $\text{tr}(\boldsymbol{\tau}'_p)$  are the important variables to be analyzed using SPOD.

We perform SPOD analyses of the perturbation fields  $u'_y$ ,  $u'_x$ , and  $\text{tr}(\boldsymbol{\tau}'_p)$  separately due to the intense memory requirements of the algorithm of Schmidt (2022). However, for a small dataset ( $N_t = 4000$ ,  $N_o = 125$ ), we have also calculated the SPOD spectrum of the velocity components together, which shows that the main characteristics of SPOD spectra remain unchanged (Appendix B). As will be shown, the spectral characteristics arising from each separate analysis are highly consistent, displaying peaks at the same frequencies. It is possible in principle, though highly memory intensive, to perform SPOD on the entire velocity and stress (or conformation) field, by extending the framework presented for POD by Wang *et al.* (2014). As indicated there, as well as in Hameduddin & Zaki (2019), some subtleties arise in working with tensors such as  $\boldsymbol{\alpha}$  that are constrained to be positive definite.

SPOD eigenvalue spectra as a function of frequency for the first several modes in  $u'_y$ ,  $u'_x$ , and  $\text{tr}(\boldsymbol{\tau}'_p)$  are shown in Fig. 3a, Fig. 3b, and Fig. 3c, respectively, along with the sum of eigenvalues of all the modes. For velocity components, the eigenvalue represents the kinetic energy as mentioned earlier and the total kinetic energy can be represented by the SPOD amplitude as  $\|a\|^2$  (Eq. 2.8). The leading modes in wall-normal velocity and streamwise velocity contain most of the energy ( $\approx 73\%$  and  $\approx 55\%$ , respectively) and hence dominate the flow structure (Figs. 3a and 3b). In the eigenvalue spectrum of  $\text{tr}(\boldsymbol{\tau}'_p)$ , the leading mode has a relatively smaller contribution ( $\approx 31\%$ ) to  $\|a\|^2$  (Fig. 3c). The leading modes of wall-normal velocity and streamwise velocity contain distinct sharp peaks at specific frequencies, of which the first few are indicated with red symbols, and the energy of these peaks decreases as the frequency increases. The leading mode of the polymer stress field also has peaks at the same frequencies; they are not as sharp as the peaks for the velocity components but still quite distinct, as revealed by plotting on a linear scale (inset). The higher-order modes do not have such distinct peaks. The energy decay of velocity fluctuations in the SPOD spectra at a large frequency ( $f > 1$ ) approximately follows a ‘‘power law’’  $f^{-5.2}$ , which is somewhat close to the result  $f^{-14/3}$  reported by Dubief *et al.* (2013). The SPOD spectrum of  $\text{tr}(\boldsymbol{\tau}'_p)$  follows a different power law ( $f^{-3.4}$ ). The significance of these is unclear as they are only observed over less than a decade in frequency; we report them here only for completeness.

The local peaks in the energy spectrum of velocity components indicate that the structures

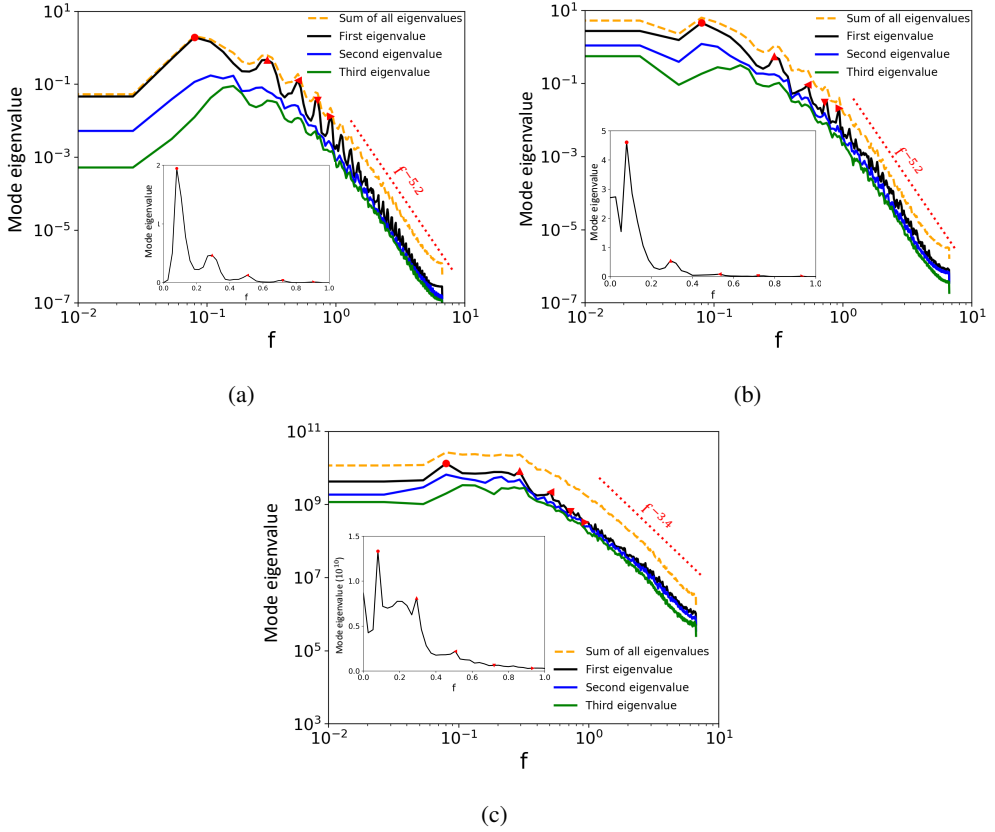


Figure 3: SPOD eigenvalue spectra of perturbations of (a) wall-normal velocity ( $u'_y$ ), (b) streamwise velocity ( $u'_x$ ), and (c) trace of polymer stress tensor ( $\text{tr}(\tau'_p)$ ) at  $Re = 3000$  and  $Wi = 35$ . Red symbols indicate the first few peaks in the leading mode of the eigenvalue spectra. Insets: SPOD eigenvalue spectra of the leading SPOD modes on a linear scale.

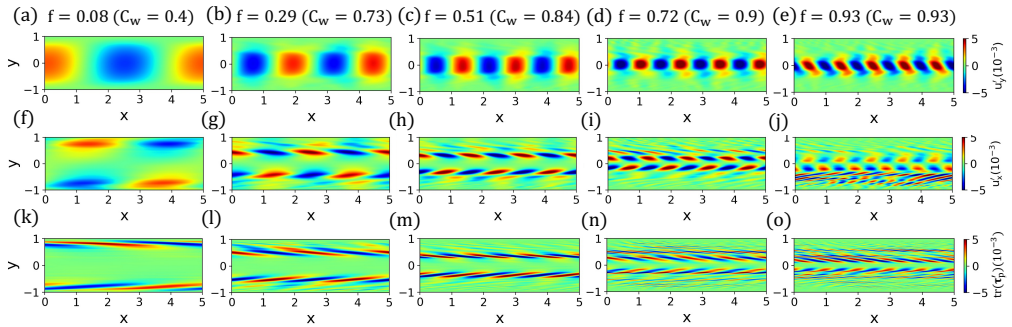


Figure 4: Structures of SPOD modes of (a-e)  $u'_y$ , (f-j)  $u'_x$ , and (k-o)  $\text{tr}(\tau'_p)$  at  $Re = 3000$  and  $Wi = 35$ ; i.e., corresponding to the frequencies denoted by different symbols in the eigenvalue spectra (Figs. 3a, 3b, and 3c).



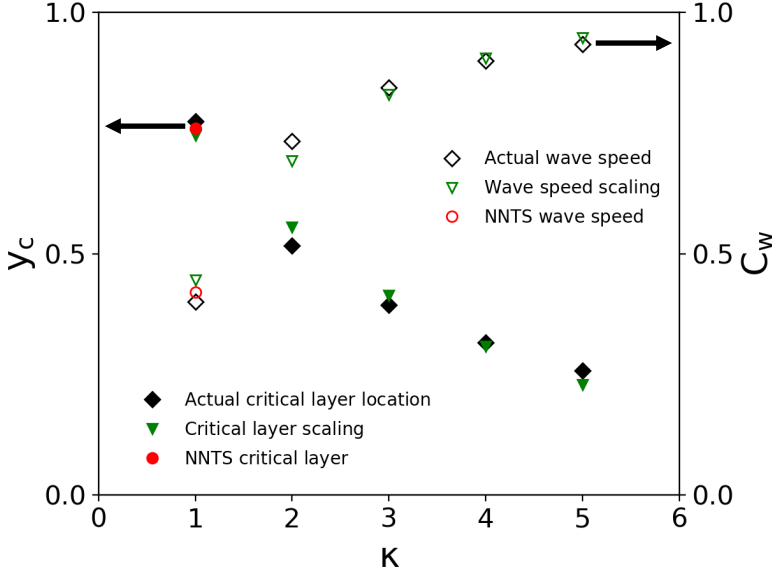


Figure 5: Wave speed and location of the critical layer at  $Re = 3000$  and  $Wi = 35$  for the traveling waves associated with the peaks in the leading SPOD mode along with the Newtonian nonlinear Tollmien–Schlichting (NNTS) wave results and the predictions of the scaling model Eqs. 3.2 and 3.3.

corresponding to these frequencies have distinct features in the dynamics of EIT. These peaks are *not* at integer multiples of the lowest-frequency peak, so are not simply harmonics; the relationship between them is elucidated below. The SPOD mode structures of  $u'_y$ ,  $u'_x$ , and  $\text{tr}(\boldsymbol{\tau}'_p)$  corresponding to the peak frequencies in the leading SPOD mode have been shown in Fig. 4. Each mode structure has a distinct wavenumber  $\kappa$ , which we measure in wavelengths per domain length. These modes are all traveling waves with wave speed  $C_w = fL/\kappa$ , as further discussed below.

The most dominant SPOD structure ( $f = 0.08$ ) has unit wavenumber ( $\kappa = 1$ ). The wall-normal velocity component for this mode consists of large-scale structures spanning the channel (Fig. 4a), the streamwise velocity component has regions of positive and negative velocity fluctuations close to the walls (Fig. 4f), and the polymer stress field displays thin layers close to the walls having inclined alternating sheets of positive and negative stress fluctuations (Fig. 4k). The structures approximately obey a shift-reflect symmetry: i.e.  $u_y(x, y) \approx -u_y(x + L/2, -y)$ ,  $u'_x(x, y) \approx u'_x(x + L/2, -y)$ , and  $\text{tr}(\boldsymbol{\tau}'_p)(x, y) \approx \text{tr}(\boldsymbol{\tau}'_p)(x + L/2, -y)$ . The quantification of the shift-reflect symmetry of different SPOD mode structures has been given in Appendix C. This is the symmetry obeyed by the TS mode (Drazin & Reid 1981), and comparison to Figure 2 indicates a strong similarity in structure. From here onward, we refer to the regions having positive and negative  $u'_y$  as “positive lobe” and “negative lobe”, respectively. The mode structures corresponding to other peaks have similar structures, where the wavenumber of structures increases with frequency (Fig. 4). The wall-normal extent of the lobes in  $u'_y$  decreases and the regions of velocity fluctuations in  $u'_x$  approach the centerline of the channel as the wavenumber increases. Relatedly, the layers of strong  $\text{tr}(\boldsymbol{\tau}'_p)$  move away from the wall as the frequency increases.

The wave speeds of the traveling structures in the leading SPOD mode are shown in Figure 5. They initially increase with the wavenumber (and frequency) and ultimately approach a

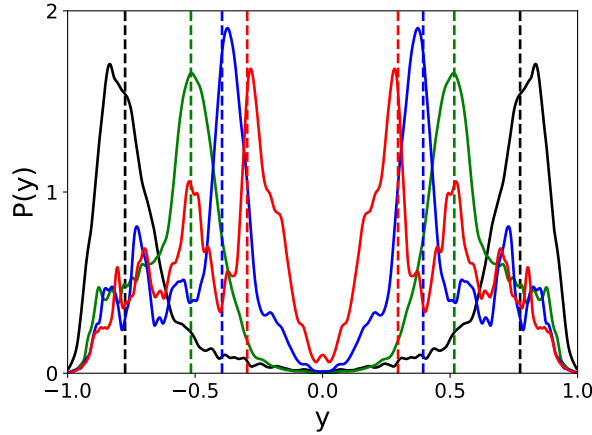


Figure 6: Wall-normal distribution of polymer stress fluctuations  $P(y)$  (solid lines) and the positions of critical layers (dashed lines) for traveling modes having wave speed  $C_w = 0.4$  (black),  $C_w = 0.73$  (green),  $C_w = 0.84$  (blue), and  $C_w = 0.9$  (red) at  $Re = 3000$  and  $Wi = 35$ .

value close to the centerline velocity of the channel ( $C_w \rightarrow 0.94$ ). The wave speed of the dominant mode structure ( $f = 0.08$ ,  $\kappa = 1$ ) is very close to that of the Newtonian nonlinear TS (NNTS) wave at the corresponding  $Re$  ( $C_{TS} = 0.42$ ), shown in red on Figure 5, further strengthening the evidence connecting EIT to the TS mode. The NNTS wave belongs to the stable (in 2D) upper branch of the nonlinear traveling wave solution of plane Poiseuille flow, which originates at  $Re = 5772$  through a subcritical bifurcation from the laminar branch and exists down to  $Re \approx 2800$  (Jiménez 1990; Shekar *et al.* 2020). By contrast, a center mode would have a wave speed close to unity and thus a frequency close to  $\kappa/L$ . For  $L = 5$  this would be multiples of 0.2, and Figure 3a shows no peaks at these positions. In fact,  $f = 0.2$  and its multiples are close to local minima in energy for the dominant SPOD mode. In short, we see no evidence of a center mode structure. The origin of the peak positions in Figure 3a is elucidated below.

As discussed in the Introduction, corresponding to the wave speed of a perturbation there is a critical layer position  $y_c$ . As this is the position where the fluid and the perturbation are moving together, it is the most favorable position for the two to exchange energy. The velocity fluctuations in EIT are very weak so we can approximate the local streamwise velocity with the laminar value,  $u_x \approx 1 - y^2$ , and the location of critical layers (i.e. where  $C_w = u_x$ ) can be given as  $y_c \approx \pm\sqrt{1 - C_w}$ . Figure 5 shows the critical layer positions corresponding to the wave speeds of the traveling structures of the leading SPOD mode, as well as for the NNTS mode. As with wave speed, the critical layer position of the  $f = 0.08$ ,  $\kappa = 1$  SPOD mode is very close to that of the NNTS mode.

To illustrate the relation between the critical layer and the location of the peaks in the SPOD stress fluctuation structures, in Figure 6 we plot the positions of the critical layers for the traveling structures of the leading SPOD mode at the first several peak frequencies, along with the wall-normal distribution of polymer stress fluctuations ( $P(y)$ ), which has been defined as

$$P(y) = \left[ \frac{\int_0^L \{\text{tr}(\boldsymbol{\tau}'_p)\}^2 dx}{\int_{-1}^1 \int_0^L \{\text{tr}(\boldsymbol{\tau}'_p)\}^2 dx dy} \right]^{1/2}. \quad (3.1)$$

The peak regions in  $P(y)$  represent the locations of the sheets of polymer stress fluctuations, and we see that their locations correspond to the critical layers. A similar observation has been made for viscoelasticity-modified TS waves and it has been reported that thin sheets of high polymer stress emanate from the critical layers of TS waves (Shekar *et al.* 2019; Hameduddin *et al.* 2019).

We noted above that as the wavenumber increases,  $u'_y$  becomes more localized toward the channel center, as do the critical layer positions where the stress fluctuations are high. More specifically, consider the  $u'_y$  profile at the second peak ( $f = 0.29$ , Figure 4b) and the  $\text{tr}(\boldsymbol{\tau}'_p)$  profile at the first peak ( $f = 0.08$ , Figure 4k). It appears that the “lobes” where  $u'_y$  is large in the former figure are roughly bounded by the layers where  $\text{tr}(\boldsymbol{\tau}'_p)$  is large in the latter. Similar observations can be made about all of the succeeding modes. We visualize this point in Figure 7, which replots the results of Figure 4 by showing contour lines of  $u'_y$  from the SPOD modes at wavenumber  $\kappa + 1$  juxtaposed with color contours of  $\text{tr}(\boldsymbol{\tau}'_p)$  at wavenumber  $\kappa$ . From this figure, we see that the velocity lobes at wavenumber  $\kappa + 1$  are “nested” within the stress fluctuations, or equivalently between the upper and lower critical layer positions, at wavenumber  $\kappa$ . In contrast, the regions between the critical layers and the channel walls contain small-scale and irregular structures both in the velocity field as well as stress field.

We now present a simple theory for the results in Fig. 5 that is motivated by the above structural observations. The nested nature of the structures revealed by SPOD suggests that the locations of the polymer sheets of a slow-moving (low wavenumber) traveling wave act like “walls” for the immediately faster-moving (and higher wavenumber) wave. Consider the existence of a “primary” mode with wave speed  $C_{w,1}$  and thus critical layer positions  $y_{c,1} = \pm(1 - C_{w,1})^{1/2}$ . We take the next higher mode to occupy the domain  $|y| < |y_{c,1}|$ ; if its critical layer position  $y_{c,2}$  is at the same fractional position in this new domain, it will thus be at  $\pm|y_{c,1}|^2 = \pm(1 - C_{w,1})^1$ . Continuing in this way, and noting that successively higher-speed waves can be labeled by their wavenumber  $\kappa$ , we have a simple scaling result

$$y_{c,\kappa} = (1 - C_{w,1})^{\kappa/2}. \quad (3.2)$$

Relatedly, the successive wave speeds are then

$$C_{w,\kappa} = 1 - (1 - C_{w,1})^\kappa. \quad (3.3)$$

Using the SPOD results for  $y_{c,\kappa}$  to find a best-fit value of  $C_{w,1}$  yields predictions for  $y_{c,\kappa}$  and  $C_{w,\kappa}$  that agree very closely with the data, as shown in Figure 5. Furthermore, the value of  $C_{w,1} = 0.44$  is very close to the NNTS wave speed  $C_{TS} = 0.42$ . These observations indicate that the structure of EIT is dominated by nested self-similar structures that closely resemble TS waves.

Finally, we briefly hypothesize a possible physical mechanism for the appearance of this nested structure. A highly stretched elastic sheet resists lateral deformation. Similarly, flows in which polymer molecules are strongly stretched along one direction resist deformations transverse to that direction. A classical example of this mechanism is the suppression of shear-layer instability in a viscoelastic fluid, where the strong stretching in the shear layer mimics an elastic sheet (Azaiez & Homay 2006). Relatedly, viscoelastic Taylor-Couette instability is suppressed by the normal stress induced by axial flow (Graham 1998), and in porous media flows, sheetlike regions with high polymer stress resist the flow passing through them and hence act like flow barriers (Kumar *et al.* 2023).

A similar mechanism may be at work here, in which the sheets of high polymer stress in the critical layers from the primary mode prevent velocity fluctuations from the higher modes from passing through the critical layer, acting as “walls” as noted above, and so on successively with the higher modes, leading to the emergence of a nested family of traveling waves. The resemblance of the SPOD mode structure in the reconstructed polymer stress

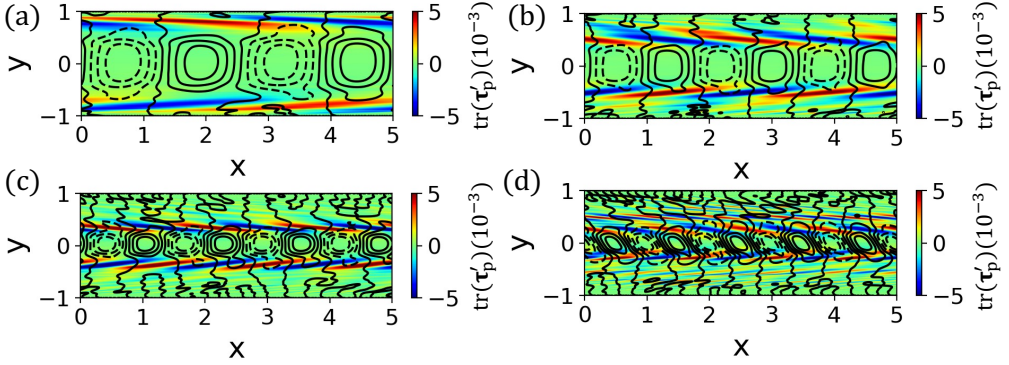


Figure 7: Contours of velocity fluctuations ( $u'_y$ ) of a faster-traveling wave on the top of the stress fluctuations of the immediate slower traveling wave: (a) stress at  $C_w = 0.4$  and velocity at  $C_w = 0.73$ , (b) stress at  $C_w = 0.73$  and velocity at  $C_w = 0.84$ , (c) stress at  $C_w = 0.84$  and velocity at  $C_w = 0.9$ , and (d) stress at  $C_w = 0.9$  and velocity at  $C_w = 0.93$ . Other parameters are  $Re = 3000$  and  $Wi = 35$ .

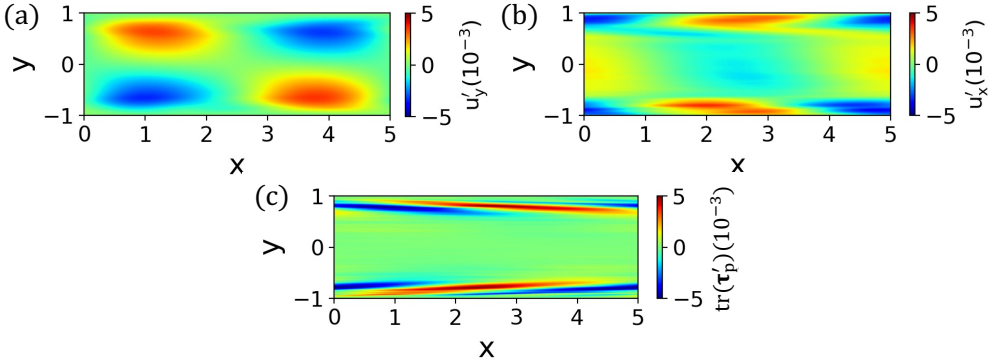


Figure 8: Mode structures of the second-most energetic mode at  $f = 0.08$ ; (a)  $u'_y$ , (b)  $u'_x$ , and (c)  $\text{tr}(\tau'_p)$ . Other parameters are  $Re = 3000$  and  $Wi = 35$

field can be seen in Appendix D. Regardless of the detailed physical mechanism, the excellent agreement between the simulation results and the scaling theory manifested in Eqs. (3.2)-(3.3) indicates the predictive power of the simple structural picture of nested traveling waves with critical layer fluctuations that define the length scale of the nesting.

For completeness, we also report in Figure 8 the structures corresponding to the second-most energetic mode from SPOD (blue curves on Figure 3) at  $f = 0.08$ . Note that the energy of this mode is substantially smaller than that of the leading mode and that the spectrum of this structure does not contain distinct peaks. This mode also has  $\kappa = 1$  and thus the same wave speed and critical layer position as the most energetic mode. It again exhibits localized polymer stretch fluctuations in the critical layer, but now displays simple reflection symmetry rather than the shift-reflect symmetry of the dominant mode. We view this as a higher-order correction on the dominant structure elucidated above.

Results obtained for ( $Re = 3000, Wi = 70$ ) and ( $Re = 6000, Wi = 35$ ) display nearly identical features to the case considered above ( $Re = 3000, Wi = 35$ ). The leading modes of the SPOD energy spectra of  $u'_y$  at different  $Wi$  and  $Re$  have been shown in Fig. 9a and Fig. 9b, respectively. The SPOD spectra of other state variables have peaks exactly at the same

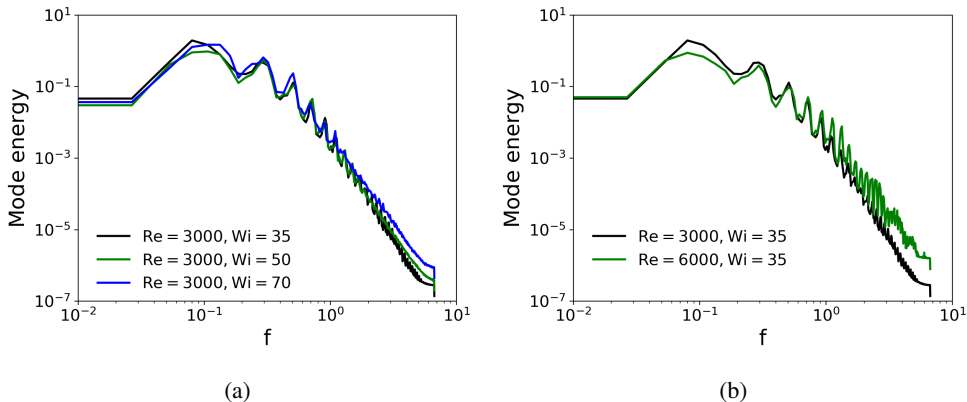


Figure 9: Leading modes of SPOD energy spectra of  $u'_y$  at different (a)  $Wi$  at  $Re = 3000$  and (b)  $Re$  at  $Wi = 35$ .

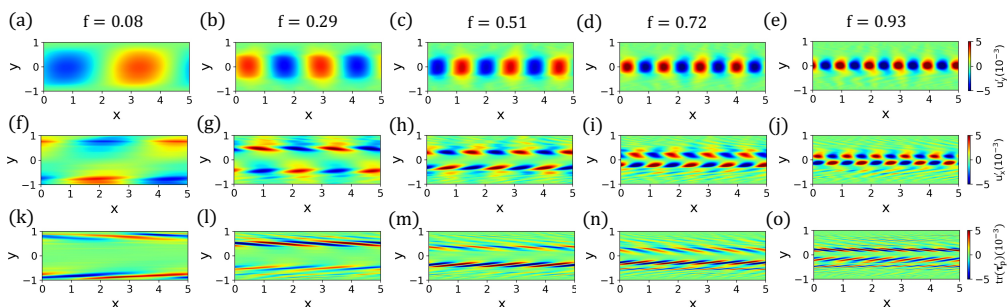


Figure 10: Structures of SPOD modes of (a-e)  $u'_y$ , (f-j)  $u'_x$ , and (k-o)  $\text{tr}(\tau'_p)$  at the peak frequencies in the leading mode of  $u'_y$  at  $Re = 6000$  and  $Wi = 35$ .

frequencies as the spectrum of  $u'_y$ . Hence, they do not provide any additional information. As  $Wi$  increases, the region close to the first peak in the SPOD spectrum becomes slightly flatter. We do not see any significant effect of  $Wi$  on the peak frequencies in the SPOD spectra, which suggests that  $Wi$  does not have any noticeable impact on the qualitative nature of the traveling structures. As  $Re$  increases, the mode energy corresponding to the lower wavenumber peaks decreases, whereas the energy corresponding to the higher wavenumber peaks increases. However, the frequencies corresponding to the peaks in the SPOD spectra remain unchanged indicating that the speed of the traveling wave is independent of  $Re$ . We also plot the SPOD mode structures of  $u'_y$ ,  $u'_x$ , and  $\text{tr}(\tau'_p)$  at the frequencies corresponding to the peaks in the leading SPOD mode at  $Re = 6000$  (Fig. 10). The mode structures of the traveling waves at  $Re = 6000$  are qualitatively similar to the structures at  $Re = 3000$  (Fig. 4).

At  $Re$  relevant to the present study, EIT overwhelmingly represents the MDR state (Lopez *et al.* 2019). Hence, the self-sustaining chaotic nature of the MDR state and its dynamics can be explained by the EIT. As noted earlier, the dynamics of EIT in both 3D channel and pipe flows are fundamentally two-dimensional (Sid *et al.* 2018; Lopez *et al.* 2019); specifically, 2D finite amplitude perturbations are self-sustaining. Therefore, it is expected, and observed (Shekar *et al.* 2019), that EIT even 3D flows would contain traveling waves originating from wall modes similar to the 2D channel flow considered in the present study. At larger  $Re$ , the MDR state may not be fully dominated by 2D EIT, and 3D flow structures may arise in that scenario. An important direction for future work will be to apply SPOD to the full 3D case.

#### 4. Conclusions

In the present study, we use Spectral Proper Orthogonal Decomposition (SPOD) to elucidate the structure underlying the chaotic dynamics of two-dimensional elastoinertial turbulence in channel flow. The most energetic mode of SPOD spectrum has distinct peaks. The mode structures corresponding to these peaks exhibit a family of well-defined traveling structures, where the velocity field contains large-scale regular patterns and the polymer stress field contains the formation of thin inclined sheets of high and low stress at the critical layers of the wave. The structure of the most dominant traveling wave (first mode, highest peak) of this family exhibits shift-reflect symmetry and resembles the structure of the Tollmien–Schlichting wave indicating its origin in a nonlinearly self-sustained wall mode. The traveling structures corresponding to the higher frequency peaks have very similar structure and symmetry, however, their wavenumber increases, and the size of large-scale structures decreases. It appears that the localized polymer sheets at the critical layers of the leading SPOD mode at a given peak frequency act like walls for the traveling structure of the mode corresponding to the next peak, and hence lead to a nested arrangement of the waves. Based on this observation, a simple theory quantitatively captures the relationship between the wave speeds and the locations of critical layers for different waves. From this analysis, a picture emerges of two-dimensional EIT as a nested collection of nonlinearly self-sustaining TS-wave-like structures.

#### Acknowledgments

This research was supported under grant ONR N00014-18-1-2865 (Vannevar Bush Faculty Fellowship). We are grateful to Aaron Towne for helpful discussions and Oliver Schmidt for making available his SPOD code.

#### Declaration of Interests

The authors report no conflict of interest.

#### Appendix A. Effect of block size and overlap on SPOD spectra

To investigate the effect of the block size ( $N_f$ ) and overlap on the estimation of SPOD spectra, we plot the SPOD spectra of  $u'_y$  obtained using different block sizes and overlaps (Fig. 11). We do not see any noticeable difference between the peaks in the SPOD spectra obtained using  $N_f = 500$  with 50% overlap in the main text (Fig. 3a) and the spectra obtained using different combinations of  $N_f$  and overlap (Fig. 11).

#### Appendix B. SPOD estimation of velocity components together

For a small dataset ( $N_t = 4000$ ) and lower overlap (25%), we have calculated the SPOD spectrum of velocity components altogether (Fig. 12). The peaks in the leading mode are exactly at the same frequencies as the SPOD calculated for each velocity component separately (Figs. 3a and 3b).

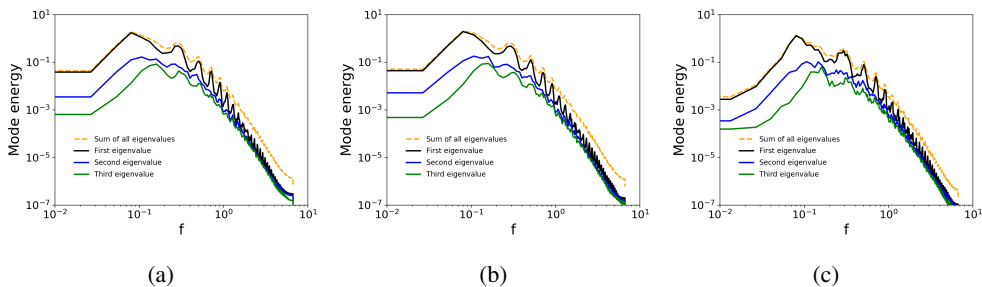


Figure 11: SPOD energy spectra of  $u'_y$  at  $Re = 3000$  and  $Wi = 35$  estimated using (a) block size  $N_f = 500$  with 25% overlap, (b) block size  $N_f = 500$  with 75% overlap, and (c) block size  $N_f = 1000$  with 50% overlap.

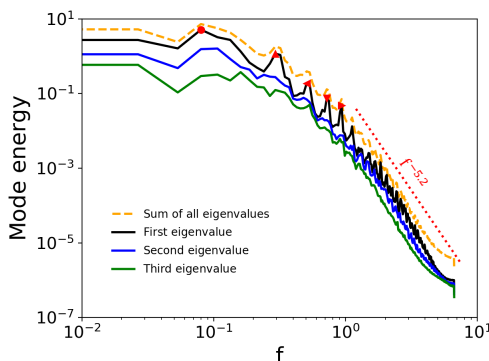


Figure 12: SPOD energy spectrum of the velocity field ( $u'_x$  and  $u'_y$  together) at  $Re = 3000$  and  $Wi = 35$  estimated using  $N_t = 4000$  with 25% overlap.

---

$f/R$	$f = 0.08$	$f = 0.29$	$f = 0.51$	$f = 0.72$	$f = 0.93$
$u'_y$	0.003	0.009	0.004	0.041	0.158
$u'_x$	0.058	0.034	0.038	0.211	0.394
$\text{tr}(\boldsymbol{\tau}'_p)$	0.304	0.089	0.057	0.336	0.397

---

Table 1: Values of shift-reflect symmetry value  $R$  (Eq. C 1) for SPOD of various quantities and modes.

---

### Appendix C. Quantification of the symmetry of SPOD mode structures

To quantify the shift-reflect symmetry of the SPOD mode structures, we define a parameter  $R$  as:

$$R = \frac{\|A(x, y) - B(x, y)\|^2}{4\|A(x, y)\|^2}, \quad (\text{C } 1)$$

where  $A(x, y)$  represents SPOD structures ( $u'_y$ ,  $u'_x$ , and  $\text{tr}(\boldsymbol{\tau}'_p)$ ) and  $B(x, y)$  represents their shift-reflect image.  $R = 0$  and  $R = 1$  represent perfect shift-reflect symmetry and reflect symmetry, respectively. The small values of  $R$  confirm that the SPOD structures obey shift-reflect symmetry (Table 1). The value of  $R$  for  $\text{tr}(\boldsymbol{\tau}'_p)$  is relatively larger than  $u'_y$ , because the SPOD modes of  $\text{tr}(\boldsymbol{\tau}'_p)$  are characterized by thin sheets and even a slight misalignment between sheets leads to a larger value of  $R$ .

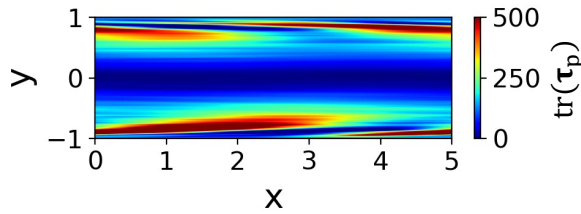


Figure 13: Reconstruction of  $\text{tr}(\tau_p)$  just using the most dominant SPOD mode (first mode, highest peak) at  $Re = 3000$  and  $Wi = 35$ .

#### Appendix D. Reconstruction of polymer stress field using specific SPOD mode

To visualize the signature of the SPOD structure in the polymer stress field, we plot the reconstruction of the polymer stress field just using the most dominant SPOD mode (first mode, highest peak) (Fig. 13). In the reconstructed stress field, we see the existence of thin sheets characterized by large polymer stress.

#### REFERENCES

- ARAYA, DANIEL B., COLONIUS, TIM & DABIRI, JOHN O. 2017 Transition to bluff-body dynamics in the wake of vertical-axis wind turbines. *Journal of Fluid Mechanics* **813**, 346–381.
- AZAIÉZ, J & HOMSÝ, G M 2006 Linear stability of free shear flow of viscoelastic liquids. *Journal of Fluid Mechanics* **268** (-1), 37–69.
- BENEITEZ, MIGUEL, PAGE, JACOB, DUBIEF, YVES & KERSWELL, RICH R. 2024 Multistability of elasto-inertial two-dimensional channel flow. *Journal of Fluid Mechanics* **981**, A30, arXiv: 2308.11554.
- BENEITEZ, MIGUEL, PAGE, JACOB & KERSWELL, RICH R. 2023 Polymer diffusive instability leading to elastic turbulence in plane Couette flow. *Physical Review Fluids* **8** (10), L101901, arXiv: 2210.09961.
- BOUCHENAF, WALID, DEWALS, BENJAMIN, LEFEVRE, ARNAUD & MIGNOT, EMMANUEL 2021 Water Soluble Polymers as a Means to Increase Flow Capacity: Field Experiment of Drag Reduction by Polymer Additives in an Irrigation Canal. *Journal of Hydraulic Engineering* **147** (8), 1–9.
- BRAUD, CAROLINE, HEITZ, DOMINIQUE, ARROYO, GEORGES, PERRET, LAURENT, DELVILLE, JOËL & BONNET, JEAN-PAUL 2004 Low-dimensional analysis, using POD, for two mixing layer–wake interactions. *International Journal of Heat and Fluid Flow* **25** (3), 351–363.
- BROSTOW, WITOLD 2008 Drag reduction in flow: Review of applications, mechanism and prediction. *Journal of Industrial and Engineering Chemistry* **14** (4), 409–416.
- BURNS, KEATON J., VASIL, GEOFFREY M., OISHI, JEFFREY S., LECOANET, DANIEL & BROWN, BENJAMIN P. 2020 Dedalus: A flexible framework for numerical simulations with spectral methods. *Physical Review Research* **2** (2), 023068, arXiv: 1905.10388.
- BUZA, GERGELY, BENEITEZ, MIGUEL, PAGE, JACOB & KERSWELL, RICH R. 2022 Finite-amplitude elastic waves in viscoelastic channel flow from large to zero Reynolds number. *Journal of Fluid Mechanics* **951**, A3, arXiv: 2202.08047.
- CHOUËIRI, GEORGE H., LOPEZ, JOSE M., VARSHNEY, ATUL, SANKAR, SARATH & HOF, BJÖRN 2021 Experimental observation of the origin and structure of elastoinertial turbulence. *Proceedings of the National Academy of Sciences* **118** (45), e2102350118, arXiv: 2103.00023.
- COUCHMAN, MILES M.P., BENEITEZ, MIGUEL, PAGE, JACOB & KERSWELL, RICH R 2024 Inertial enhancement of the polymer diffusive instability. *Journal of Fluid Mechanics* **981**, A2, arXiv: 2308.14879.
- DATTA, SUJIT S., ARDEKANI, AREZOO M., ARRATIA, PAULO E., BERIS, ANTONY N., BISCHOFBERGER, IRMGARD, MCKINLEY, GARETH H., EGGERS, JENS G., LÓPEZ-AGUILAR, J. ESTEBAN, FIELDING, SUZANNE M., FRISHMAN, ANNA, GRAHAM, MICHAEL D., GUASTO, JEFFREY S., HAWARD, SIMON J., SHEN, AMY Q., HORMOZI, SARAH, MOROZOV, ALEXANDER, POOLE, ROBERT J., SHANKAR, V., SHAQFEH, ERIC S. G., STARK, HOLGER, STEINBERG, VICTOR, SUBRAMANIAN, GANESH & STONE, HOWARD A. 2022 Perspectives on viscoelastic flow instabilities and elastic turbulence. *Physical Review Fluids* **7** (8), 080701, arXiv: 2108.09841.
- DRAZIN, PG & REID, WH 1981 *Hydrodynamic stability* (cambridge university).



- DUBIEF, Y, PAGE, J, KERSWELL, R R, TERRAPON, V E & STEINBERG, V 2022 First coherent structure in elasto-inertial turbulence. *Physical Review Fluids* **7** (7), 073301.
- DUBIEF, YVES, TERRAPON, VINCENT E & HOF, BJÖRN 2023 Elasto-Inertial Turbulence. *Annual Review of Fluid Mechanics* **55** (1), 675–705.
- DUBIEF, YVES, TERRAPON, VINCENT E. & SORIA, JULIO 2013 On the mechanism of elasto-inertial turbulence. *Physics of Fluids* **25** (11), arXiv: 1301.3952.
- GARG, PIYUSH, CHAUDHARY, INDRESH, KHALID, MOHAMMAD, SHANKAR, V. & SUBRAMANIAN, GANESH 2018 Viscoelastic Pipe Flow is Linearly Unstable. *Physical Review Letters* **121** (2), 24502, arXiv: 1711.07991.
- GRAHAM, MICHAEL D 1998 Effect of axial flow on viscoelastic Taylor-Couette instability. *Journal of Fluid Mechanics* **360**, 341–374.
- GRAHAM, MICHAEL D. & FLORYAN, DANIEL 2021 Exact Coherent States and the Nonlinear Dynamics of Wall-Bounded Turbulent Flows. *Annual Review of Fluid Mechanics* **53** (1), 227–253.
- HAMEDUDDIN, ISMAIL, GAYME, DENNICE F. & ZAKI, TAMER A. 2019 Perturbative expansions of the conformation tensor in viscoelastic flows. *Journal of Fluid Mechanics* **858**, 377–406, arXiv: 1811.02501.
- HAMEDUDDIN, ISMAIL & ZAKI, TAMER A. 2019 The mean conformation tensor in viscoelastic turbulence. *Journal of Fluid Mechanics* **865**, 363–380.
- HELLSTRÖM, LEO H. O. & SMITS, ALEXANDER J. 2014 The energetic motions in turbulent pipe flow. *Physics of Fluids* **26** (12).
- JIMÉNEZ, JAVIER 1990 Transition to turbulence in two-dimensional Poiseuille flow. *Journal of Fluid Mechanics* **218** (-1), 265.
- KHALID, MOHAMMAD, CHAUDHARY, INDRESH, GARG, PIYUSH, SHANKAR, V. & SUBRAMANIAN, GANESH 2021 The centre-mode instability of viscoelastic plane Poiseuille flow. *Journal of Fluid Mechanics* **915**, A43, arXiv: 2008.00231.
- KIM, KYOUNGYOUN, LI, CHANG-F., SURESHKUMAR, R., BALACHANDAR, S. & ADRIAN, RONALD J. 2007 Effects of polymer stresses on eddy structures in drag-reduced turbulent channel flow. *Journal of Fluid Mechanics* **584**, 281–299.
- KUMAR, MANISH & GRAHAM, MICHAEL D. 2023 Effect of polymer additives on dynamics of water level in an open channel. *Journal of Non-Newtonian Fluid Mechanics* **321** (June), 105129, arXiv: 2307.00626.
- KUMAR, MANISH, GUASTO, JEFFREY S. & ARDEKANI, AREZOO M 2023 Lagrangian stretching reveals stress topology in viscoelastic flows. *Proceedings of the National Academy of Sciences* **120** (5).
- LI, WEI & GRAHAM, MICHAEL D. 2007 Polymer induced drag reduction in exact coherent structures of plane Poiseuille flow. *Physics of Fluids* **19** (8).
- LOPEZ, JOSE M, CHOUERI, GEORGE H & HOF, BJÖRN 2019 Dynamics of viscoelastic pipe flow at low Reynolds numbers in the maximum drag reduction limit. *Journal of Fluid Mechanics* **874**, 699 – 719.
- LUMLEY, JOHN LEASK 1967 The structure of inhomogeneous turbulent flows. *Atmospheric turbulence and radio wave propagation* pp. 166–178.
- MOROZOV, ALEXANDER 2022 Coherent Structures in Plane Channel Flow of Dilute Polymer Solutions with Vanishing Inertia. *Physical Review Letters* **129** (1), 017801, arXiv: 2201.01274.
- NEKKANTI, AKHIL & SCHMIDT, OLIVER T. 2021 Frequency–time analysis, low-rank reconstruction and denoising of turbulent flows using SPOD. *Journal of Fluid Mechanics* **926**, A26, arXiv: 2011.03644.
- SAMANTA, DEVRANJAN, DUBIEF, YVES, HOLZNER, MARKUS, SCHÄFER, CHRISTOF, MOROZOV, ALEXANDER N., WAGNER, CHRISTIAN & HOF, BJÖRN 2013 Elasto-inertial turbulence. *Proceedings of the National Academy of Sciences* **110** (26), 10557–10562.
- SCHMIDT, OLIVER T. 2022 Spectral proper orthogonal decomposition using multitaper estimates. *Theoretical and Computational Fluid Dynamics* **36** (5), 741–754, arXiv: 2112.10847.
- SCHMIDT, OLIVER T. & COLONIUS, TIM 2020 Guide to Spectral Proper Orthogonal Decomposition. *AIAA Journal* **58** (3), 1023–1033.
- SCHMIDT, OLIVER T. & TOWNE, AARON 2019 An efficient streaming algorithm for spectral proper orthogonal decomposition. *Computer Physics Communications* **237**, 98–109, arXiv: 1711.04199.
- SCHMIDT, OLIVER T., TOWNE, AARON, COLONIUS, TIM, CAVALIERI, ANDRÉ V. G., JORDAN, PETER & BRÈS, GUILLAUME A. 2017 Wavepackets and trapped acoustic modes in a turbulent jet: coherent structure eduction and global stability. *Journal of Fluid Mechanics* **825**, 1153–1181.
- SELLIN, R. H. J. 1978 Drag reduction in sewers: First results from a permanent installation. *Journal of Hydraulic Research* **16** (4), 357–371.

- SHEKAR, ASHWIN, McMULLEN, RYAN M., McKEON, BEVERLEY J. & GRAHAM, MICHAEL D. 2020 Self-sustained elastoinertial Tollmien–Schlichting waves. *Journal of Fluid Mechanics* **897**, A3, arXiv: 1910.11419.
- SHEKAR, ASHWIN, McMULLEN, RYAN M., McKEON, BEVERLEY J. & GRAHAM, MICHAEL D. 2021 Tollmien–Schlichting route to elastoinertial turbulence in channel flow. *Physical Review Fluids* **6** (9), 093301, arXiv: 2104.10257.
- SHEKAR, ASHWIN, McMULLEN, RYAN M., WANG, SUNG-NING, McKEON, BEVERLEY J & GRAHAM, MICHAEL D 2019 Critical-Layer Structures and Mechanisms in Elastoinertial Turbulence. *Physical Review Letters* **122** (12), 124503.
- SID, S., TERRAPON, V. E. & DUBIEF, Y. 2018 Two-dimensional dynamics of elasto-inertial turbulence and its role in polymer drag reduction. *Physical Review Fluids* **3** (1), 011301, arXiv: 1710.01199.
- TOMS, B. A. 1949 Some observations on the flow of linear polymersolutions through straight tubes at large reynolds numbers. In *Proc. 1st Intl Congr. Rheol.*, , vol. 2, pp. 135–141.
- TOWNE, AARON, SCHMIDT, OLIVER T. & COLONIUS, TIM 2018 Spectral proper orthogonal decomposition and its relationship to dynamic mode decomposition and resolvent analysis. *Journal of Fluid Mechanics* **847**, 821–867, arXiv: 1708.04393.
- TUTKUN, MURAT & GEORGE, WILLIAM K. 2017 Lumley decomposition of turbulent boundary layer at high Reynolds numbers. *Physics of Fluids* **29** (2).
- WANG, SUNG-NING, GRAHAM, MICHAEL D., HAHN, FRIEDEMANN J. & XI, LI 2014 Time-series and extended Karhunen–Loève analysis of turbulent drag reduction in polymer solutions. *AIChE Journal* **60** (4), 1460–1475, arXiv: 0201037v1.
- WELCH, P. 1967 The use of fast Fourier transform for the estimation of power spectra: A method based on time averaging over short, modified periodograms. *IEEE Transactions on Audio and Electroacoustics* **15** (2), 70–73.